Structures 69 (2024) 107379

Contents lists available at ScienceDirect

Structures

journal homepage: www.elsevier.com/locate/structures

An investigation on seismic performance of the separated fluid inerter base on model experiment and shaking table test

Yangyang Liao [a], Hesheng Tang [a,*], Taikun Guo [a], Rongshuai Li [b], Liyu Xie [a]

[a] Department of Disaster Mitigation for Structures, College of Civil Engineering, Tongji University, Shanghai 200092, China
[b] Shanghai Construction Group Co., Ltd., Shanghai 200080, China

ARTICLE INFO

Keywords:
Vibration control
Separated fluid inerter
Model experiment
FS-BIFI
Shaking table test

ABSTRACT

Fluid inerters have gained attention in structural vibration control for their simplicity, durability, high energy dissipation, and significant apparent mass amplification. This study presents an innovative design of a separated fluid inerter, which enhances inertial force, allows for more flexible installation methods, and supports a wider range of connections. A mechanical model is developed and experimentally validated for the separated fluid inerter. The effects of key design parameters on the device's mechanical properties are examined, with a focus on the radii (r_1) and length (l) of the helical tube and the radii (r_2) of hydraulic cylinder. Theoretical and experimental results confirm the model's reliability and the sensitivity of the device to these parameters. Additionally, a combination of the separated fluid inerter with anti-overturning rolling isolation is applied to a frame structure, and its seismic performance is evaluated through the shaking table test. The results indicate that the separated fluid inerter can effectively reduce the displacement of the isolation layer without significantly increasing the top floor acceleration of the frame structure equipped base isolation (FS-BI).

1. Introduction

Earthquakes, among the most prevalent and devastating natural calamities globally, present a significant peril to both human lives and property safety [1,2]. In response, structural vibration control has emerged as a modern technology developed in recent decades to enhance the safety and resilience of engineering structures against seismic events [3]. This technology finds extensive application across multiple domains, including structural engineering, bridge engineering, ocean engineering, and mechanical engineering [4–8].

The realm of structural vibration control encompasses isolation, energy dissipation, and dynamic vibration absorption technologies, delineated by distinct design concepts and control mechanisms [9–11]. Isolation technology aims to concentrate the seismic-induced deformation primarily within the isolation layer, effectively mitigating the impact of earthquakes on buildings [12]. Devices like rubber isolation bearings exemplify this approach and significantly curtail the transfer of seismic energy to the superstructure [13]. Energy dissipation technology augments structural damping and dissipates vibration energy by strategically integrating energy dissipation devices within the structure [14,15]. Recent advancements in energy dissipation technology have introduced innovations like viscoelastic dampers [16]. In order to further enhance the performance of viscoelastic dampers, Xu et al. [17–19] conducted a series of in-depth studies on the properties and stability of viscoelastic materials. The dynamic vibration absorption technology functions by introducing subsystems within the structure to facilitate the transfer of energy during structural vibration. Approaches like tuned mass dampers represent effective means to attenuate structural vibration [20].

The inerter system, a recent addition to structural vibration control technology, has garnered attention in recent years [21,22]. Central to this system, the inerter, functioning as a two-terminal acceleration-dependent element, offers inertance significantly surpassing its actual mass. The discovery of the inertance amplification effect in the 1970 s unveiled its potential for structural vibration control. Despite this, comprehensive elucidation and research into the inerter's application and damping mechanisms remained scarce for an extended period. In the early 2000 s, Ikago et al. [23,24] and Saito et al. [25] introduced the tuned viscous mass damper (TVMD), employing the principle of a ball-screw shaft, thereby unequivocally showcasing the utilization of inertance amplification.

The inertance amplification capability within inerter devices is often achieved by manipulating motion forms, such as transitioning between

* Corresponding author.
E-mail address: thstj@tongji.edu.cn (H. Tang).

https://doi.org/10.1016/j.istruc.2024.107379
Received 16 June 2024; Received in revised form 12 September 2024; Accepted 23 September 2024
Available online 26 September 2024

Nomenclature

r_1	Radius of cylinder.
r_2	Radius of helical tube.
A_1	Cross sectional area of cylinder.
A_2	Cross sectional area of helical tube.
L	Effective length of cylinder.
R	Rotation radius of helical tube.
h_d	Pitch of helical tube.
l	Length of helical tube.
n	Number of helical turns.
μ	Viscosity coefficient of liquid.
ρ	Density of the liquid.
x	Displacement of fluid in cylinder.
u	Displacement of fluid in helical tube.
F_{bch}	Inertial force of fluid in helical tube.
F_{bcy}	Inertial force of fluid in cylinder.
F_{bp}	Inertial force of piston.
F_d	Damping force of fluid flow in helical tube.
F_{in}	Damping force at inlet of helical tube.
F_{out}	Damping force at outlet of helical tube.
m_{cy}	Mass of fluid in cylinder.
m_p	Mass of piston.
m_{ch}	Mass of fluid in helical tube.
m_b	Inertance.

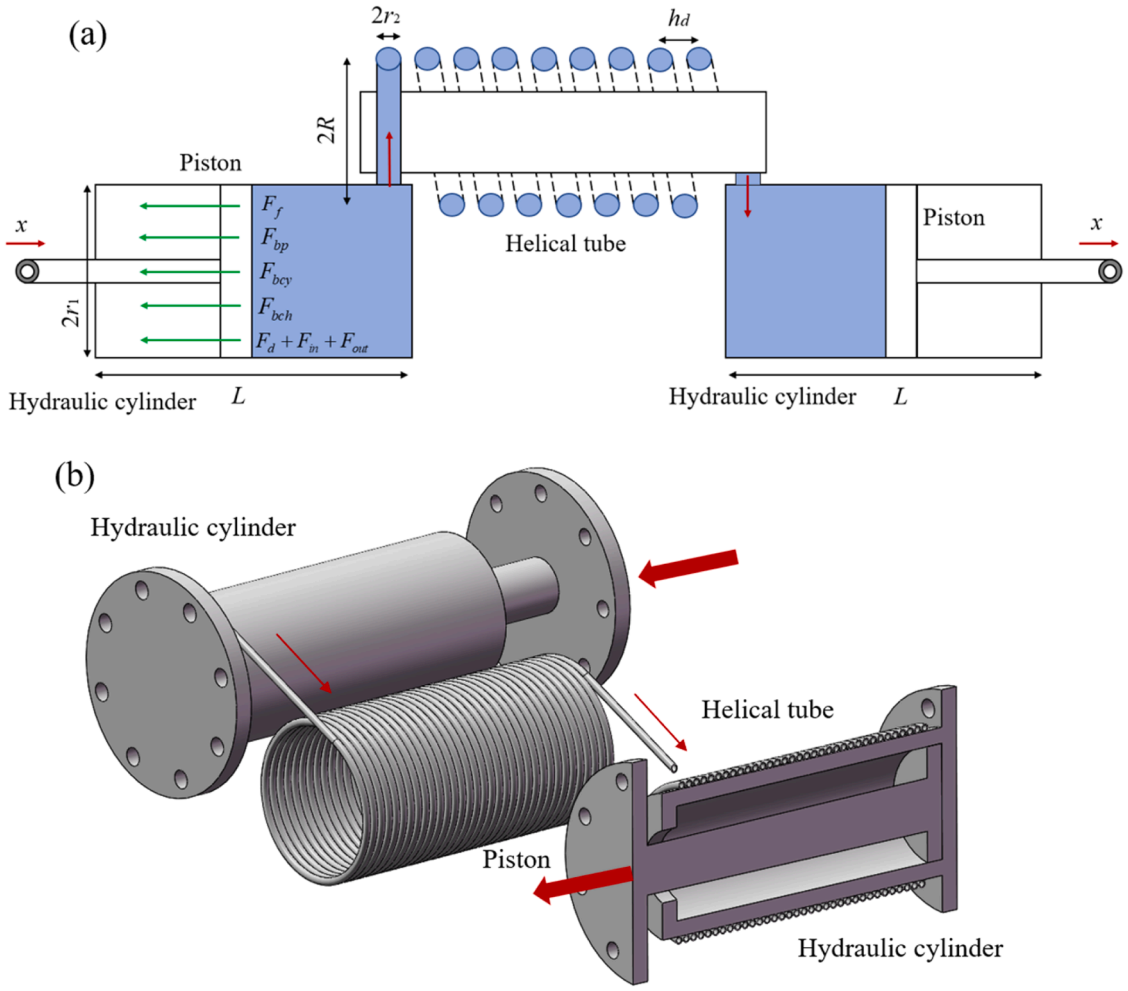

Fig. 1. Schematic diagram of the separated fluid inerter. (a) Force diagram; (b) 3D schematic diagram.

translation and rotation or altering fluid velocity [26,27]. These include the gear-rack inerter, ball-screw inerter, electromagnetic inerter, and hydraulic inerter. Smith and Wang [28] introduced a passive suspension strut based on the inerter mechanism, which uses meshing transmission among the rack, pinion, and gear to convert linear motion at both ends into rotational motion, enabling inertance amplification. Ikago et al. [29] demonstrated a mass amplifier using a ball-screw mechanism, integrating it into a seismic control device. The ball-screw component converts the linear motion of the screw into the rotational motion of the nut, which drives a flywheel to amplify rotational inertia. Additionally, Zhang et al. [30] innovated a novel crank inerter grounded in a crank mechanism. Through the use of a slider and connecting rod, translational motion is converted into flywheel rotation, thereby amplifying inertance. These studies collectively represent common mechanical inerter mechanisms.

The hydraulic inerter stands as an alternative inerter device employing hydraulic mechanisms to achieve inertance amplification. Wang et al. [31] introduced a pioneering hydraulic motor inerter,

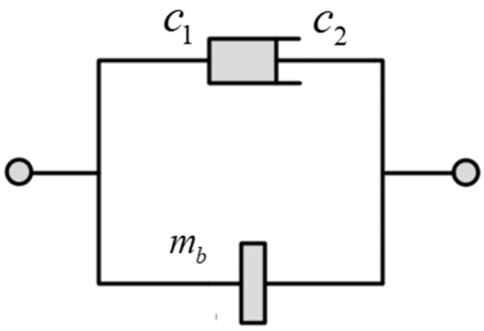

Fig. 2. Simplified model of the separated fluid inerter.

constituting a closed hydraulic system encompassing a hydraulic cylinder, hydraulic motor, and connecting pipelines. The fundamental principle revolves around creating a pressure difference between the cylinder's left and right sides via piston movement. This action propels the hydraulic motor, facilitating flywheel motion and the consequent amplification of apparent mass. In a separate study, Swift et al. [32] devised a fluid inerter comprised of a hydraulic cylinder, piston, and helical tube. The piston's motion induces fluid flow within the helical tube, leveraging the diameter difference between the tube and cylinder to amplify flow velocity and, in turn, the apparent mass. Liu et al. [33] proposed a controllable fluid inerter featuring adjustment capabilities for both inertia and damping coefficients via two electromagnetic valves, representing an enhancement over traditional fluid inerters. The inherent simplicity and durability of the fluid inerter, relying solely on liquid flow for apparent mass amplification, coupled with inherent parasitic damping to dissipate seismic energy, underscore its promising application potential.

Building upon prior research, this paper introduces an enhanced separated fluid inerter, aimed at providing heightened inertial force, expanded installation adaptability, and a more extensive range of connection options. The separation design implemented in the cylinders aims to surpass the length constraints typically associated with cylinders and mitigate the reduction in the effective working area caused by piston rod presence. This design enhancement facilitates greater piston stroke and heightened inertia force. Initially, the mechanical model of the separated fluid inerter was formulated utilizing mechanical theory, subsequently undergoing validation through model experiment. The study proceeded to investigate the influence of diverse design parameters on the mechanical characteristics of the separated inerter, integrating empirical findings with theoretical models to offer comprehensive insights into its performance. In addition, the combination of separation fluid inerter and anti-overturning rolling isolation was applied to the frame structure. The seismic performance of the frame structure equipped with the base isolation-fluid inerter (FS-BIFI)

Table 1
Performance parameters of the servo actuator.

Index	Value	Index	Value
Dynamic force	± 247 kN	Rated flow of servo valve	250 l/min
Static force	± 307 kN	Working stroke	± 150 mm
Operating pressure	280 Bar	Maximum stroke	± 190 mm

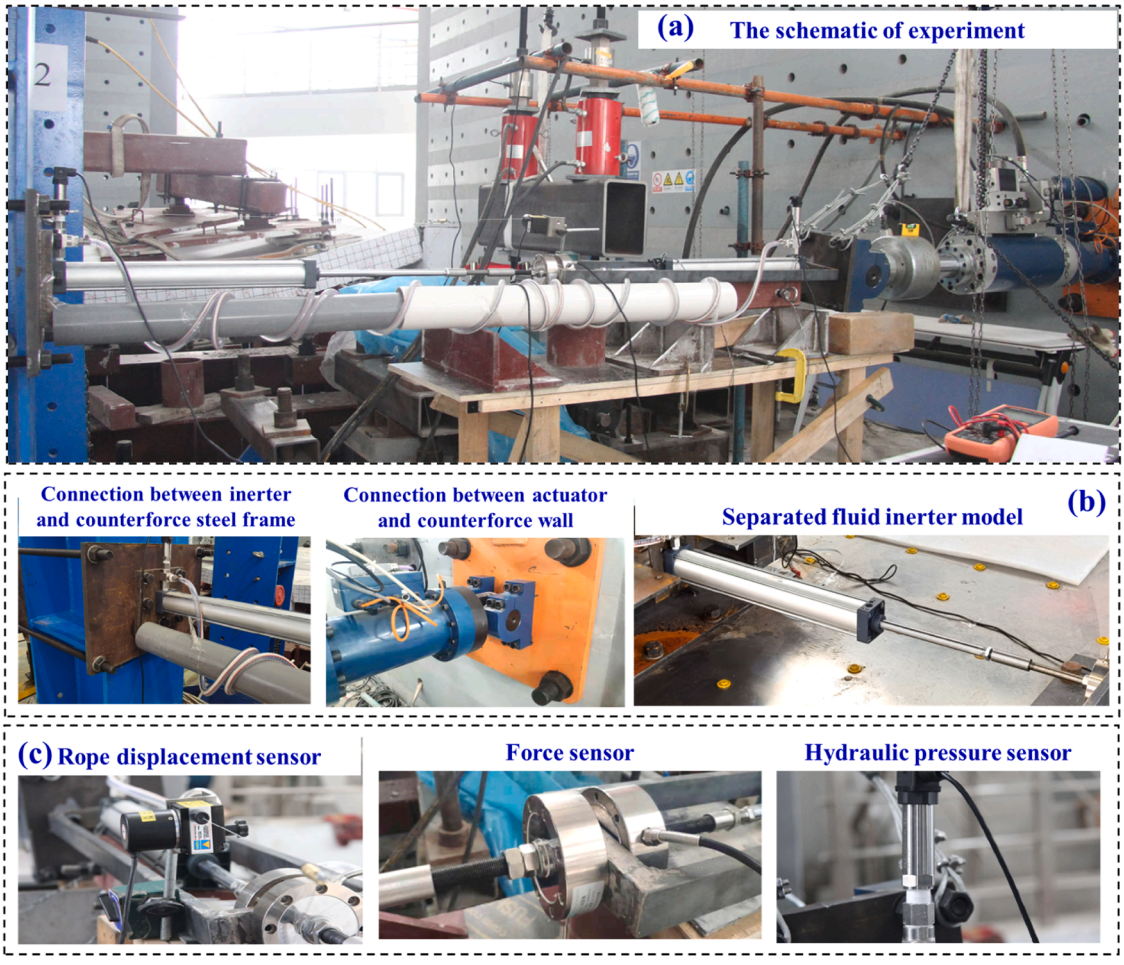

Fig. 3. The experimental devices of the separated fluid inerter. (a) The separated fluid inerter; (b) The connections; (c) The sensor.

Table 2
Dimensions of different numbered inerter models.

Model	Fluid	r_1 (mm)	r_2 (mm)	l (m)	Model	Fluid	r_1 (mm)	r_2 (mm)	l (m)
1	Empty	31.5	5	4	6	Water	31.5	15	4
2	Water	31.5	5	4	7	Water	31.5	5	5
3	Water	40	5	4	8	Water	31.5	5	6
4	Water	50	5	4	9	Water	31.5	5	7
5	Water	31.5	10	4					

was investigated by shaking table test.

2. Mechanical model of the separated fluid inerter

As illustrated in Fig. 1, the separated fluid inerter comprises a helical tube, two hydraulic cylinders, and two pistons.

The working area A_1 of the hydraulic cylinder, the working area A_2 of the helical tube, the mass m_{cy} of fluid in the hydraulic cylinder, the mass m_{ch} of fluid in the helical tube and the total length l of the helical tube are $A_1 = \pi r_1^2$, $A_2 = \pi r_2^2$, $m_{cy} = \frac{\rho l A_1}{2}$, $m_{ch} = \rho l A_2$ and $l = n\sqrt{{h_d}^2 + (2\pi \mathrm{R})^2}$ respectively.

Since the fluid is incompressible, the following equation can be obtained:

$$A_1\dot{x} = A_2\dot{u} \tag{1}$$

Where $\dot{x}$ and $\dot{u}$ represent the velocity of the fluid in hydraulic cylinder and helical tube respectively.

During the motion of the fluid inerter, the inertia force F_{bp} of two pistons can be expressed as:

$$F_{bp} = 2m_p\ddot{x} \tag{2}$$

The inertia force F_{bcy} of the fluid in two hydraulic cylinders can be expressed as:

$$F_{bcy} = 2m_{cy}\ddot{x} = \rho l A_1\ddot{x} \tag{3}$$

The substantial disparity in fluid velocity between the helical tube and the cylinders renders the kinetic energy of the fluid within the cylinders significantly lower compared to that within the helical tube, allowing it to be disregarded. Consequently, the stored energy within the inerter can be represented as:

$$E_{kch} = \frac{1}{2}m_{ch}\dot{u}^2 = \frac{1}{2}m_b\dot{x}^2 \tag{4}$$

The inertia force F_{bch} of the fluid in the helical tube can be expressed as :

$$F_{bch} = m_{ch}\ddot{u} = m_b\ddot{x} = \frac{\rho l A_1^2}{A_2}\ddot{x} \tag{5}$$

The shear friction force F_f between the piston and the inner wall of the hydraulic cylinder can be expressed as [32]:

$$F_f = \frac{4\pi\mu(r_1 - \Delta r)H}{\Delta r}\dot{x} \tag{6}$$

Where Δr is the gap width between the inner wall of the hydraulic cylinder and the piston, which can be approximately 0.1 mm.

The damping forces F_{in} and F_{out} at the inlet and outlet of the helical tube may be described as follows, with reference to the research of Massey and Ward-Smith [34]:

$$F_{in} = \Delta p_{in}A_1 = 0.25\rho A_1\left(\frac{A_1}{A_2}\right)^2\dot{x}^2 sign(\dot{x}) \tag{7}$$

$$F_{out} = \Delta p_{out}A_1 = 0.5\rho A_1\left(\frac{A_1}{A_2}\right)^2\dot{x}^2 sign(\dot{x}) \tag{8}$$

Where Δp_{in} and Δp_{out} are pressure drop at inlet and outlet, $sign(\cdot)$is the symbolic function.

The damping force F_d induced by the fluid flow within the helical tube can be expressed as [35]:

$$F_d = \Delta p_{ch}A_1 = 4f_F\frac{l}{D_h}\frac{\rho\dot{u}^2}{2}A_1 sign(\dot{x}) \tag{9}$$

Where f_F is Fanning friction factor, which can be calculated by referring to the different empirical models in [35–41]. This paper adopts the empirical formula proposed by White [36], namely:

$$f_F = 0.08\mathrm{Re}^{-0.25} + 0.012\sqrt{\frac{r_2}{r_3}} \tag{10}$$

Where Re is Reynolds Number. Therefore, the damping force F_d can be expressed as:

$$\begin{aligned} F_d &= \left(0.0160\frac{\rho l}{R^{0.5}}\frac{A_1^3}{A_2^{2.25}}\dot{x}^2 + 0.1376\mu^{0.25}\rho^{0.75}l\frac{A_1^{2.75}}{A_2^{2.375}}|\dot{x}|^{1.75}\right)sign(\dot{x}) \\ &= \left(c_1\dot{x}^2 + c_2|\dot{x}|^{1.75}\right)sign(\dot{x}) \end{aligned} \tag{11}$$

Where c_1 and c_2 are different damping coefficients. Due to the complexity of the damping force, the two damping coefficients will be determined based on the results in subsequent experiments.

Therefore, the mechanical model of separated fluid inerter can be expressed as:

$$F_{total} = F_f + F_{in} + F_{out} + F_d + F_{bp} + F_{bch} + F_{bcy} \tag{12}$$

According to Eqs. (2), (3) and (5), the following equations can be obtained:

$$\frac{F_{bch}}{F_{bcy}} = \frac{\rho l\frac{A_1^2}{A_2}}{\rho l A_1} = \frac{lA_1}{LA_2} = \frac{l}{L}\left(\frac{r_1}{r_2}\right)^2 \tag{13}$$

$$\frac{F_{bch}}{F_{bp}} = \frac{\rho l A_1^2}{m_p A_2} = \frac{m_{cy}}{m_p}\frac{A_1}{A_2}\frac{l}{L} \tag{14}$$

Normally, $A_1/A_2 > 100$ and $l/L > 10$, so the inertia force F_{bp} exerted by the pistons and the inertia force F_{bcy} associated with the fluid in the hydraulic cylinders are negligible when contrasted with the inertia force F_{bch} within the helical tube. Consequently, the mechanical model of the separated fluid inerter can be streamlined into a parallel configuration featuring an inertance element and a nonlinear damping element, depicted in Fig. 2, manifesting as:

$$F_{total} \approx F_d + F_{bch} \tag{15}$$

3. Performance analysis based on model experiment

3.1. Experimental details

To validate the accuracy of the aforementioned theoretical model, an experimental investigation was conducted to assess the mechanical characteristics of the separated fluid inerter, aiming to delve deeper into its operational mechanisms. All tests are completed in *Open Experimental Base of Hohai University* (see Fig. 3). The separated fluid inerter model is

Table 3
The unique test conditions of 9 fluid inerter models.

Case No.	Model No.	Loading mode	Amplitude (mm)	Frequency (Hz)
IS315 −5 −4-TRI-empty	No. 1	triangular wave	30	0.1
IS315 −5 −4-TRI	No. 2	triangular wave	30	0.1
IS315 −5 −4-SIN30 −0.1	No. 2	sinusoidal wave	30	0.1
IS315 −5 −4-SIN30 −0.5	No. 2	sinusoidal wave	30	0.5
IS315 −5 −4-SIN30 −1	No. 2	sinusoidal wave	30	1
IS315 −5 −4-SIN20 −0.5	No. 2	sinusoidal wave	20	0.5
IS315 −5 −4-SIN20 −1	No. 2	sinusoidal wave	20	1
IS315 −5 −4-SIN20 −2	No. 2	sinusoidal wave	20	2
IS315 −5 −4-SIN10 −1	No. 2	sinusoidal wave	10	1
IS315 −5 −4-SIN10 −2	No. 2	sinusoidal wave	10	2
IS315 −5 −4-SIN10 −3	No. 2	sinusoidal wave	10	3
IS40 −5 −4-TRI	No. 3	triangular wave	30	0.1
IS40 −5 −4-SIN30 −0.5	No. 3	sinusoidal wave	30	0.5
IS40 −5 −4-SIN20 −1	No. 3	sinusoidal wave	20	1
IS40 −5 −4-SIN10 −2	No. 3	sinusoidal wave	10	2
IS50 −5 −4-TRI	No. 4	triangular wave	30	0.1
IS50 −5 −4-SIN30 −0.5	No. 4	sinusoidal wave	30	0.5
IS50 −5 −4-SIN20 −1	No. 4	sinusoidal wave	20	1
IS50 −5 −4-SIN10 −2	No. 4	sinusoidal wave	10	2
IS315 −10 −4-TRI	No. 5	triangular wave	30	0.1
IS315 −10 −4-SIN30 −0.5	No. 5	sinusoidal wave	30	0.5
IS315 −10 −4-SIN20 −1	No. 5	sinusoidal wave	20	1
IS315 −10 −4-SIN10 −2	No. 5	sinusoidal wave	10	2
IS315 −15 −4-TRI	No. 6	triangular wave	30	0.1
IS315 −15 −4-SIN30 −0.5	No. 6	sinusoidal wave	30	0.5
IS315 −15 −4-SIN20 −1	No. 6	sinusoidal wave	20	1
IS315 −15 −4-SIN10 −2	No. 6	sinusoidal wave	10	2
IS315 −5 −5-TRI	No. 7	triangular wave	30	0.1
IS315 −5 −5-SIN30 −0.5	No. 7	sinusoidal wave	30	0.5
IS315 −5 −5-SIN20 −1	No. 7	sinusoidal wave	20	1
IS315 −5 −5-SIN10 −2	No. 7	sinusoidal wave	10	2
IS315 −5 −6-TRI	No. 8	triangular wave	30	0.1
IS315 −5 −6-SIN30 −0.5	No. 8	sinusoidal wave	30	0.5
IS315 −5 −6-SIN20 −1	No. 8	sinusoidal wave	20	1
IS315 −5 −6-SIN10 −2	No. 8	sinusoidal wave	10	2
IS315 −5 −7-TRI	No. 9	triangular wave	30	0.1
IS315 −5 −7-SIN30 −0.5	No. 9	sinusoidal wave	30	0.5
IS315 −5 −7-SIN20 −1	No. 9	sinusoidal wave	20	1
IS315 −5 −7-SIN10 −2	No. 9	sinusoidal wave	10	2

refitted from two standard cylinders and a slender tube. During the test, the Servotest SV250 servo actuator is used as the loading device, and its performance parameters are shown in Table 1. A total of 5 sensors are deployed during the experiment. The rope displacement sensor with a measuring range of 0–500 mm is used to measure the displacement of the pistons, and 2 force sensors with a range of 0–5000 kg and an accuracy of 0.03 % are used to measure the forces at both ends of the inerter , 2 hydraulic sensors with a range of 0–25 Mpa and an accuracy of 0.03 % are used to measure the pressure at both ends of the helical tube. Fig. 3 illustrates the connection details of all experimental devices, tailored to accommodate the model' dimensions and field conditions. IS*x-y-z-Xk-n* is the form of the loading condition label, IS represents the separated fluid inerter, x represents the radius of cylinder, y is the radius of helical tube, z is the length of helical tube, X represents sinusoidal or triangular loading, k is the amplitude of loading, n is the frequency of loading.

The experimental loading modes encompass sinusoidal and triangular waves, with amplitudes set at 10 mm, 20 mm, and 30 mm to facilitate complete fluid movement within the slender helical tube. To avert relative displacement between the cylinder and the ground due to excessive frequency during testing, the loading frequency range is confined to 0–3 Hz. A comprehensive array of 9 inerter models is designed and tested across different loading modes, amplitudes, and frequencies, detailed in Tables 2 and 3. Model 1 is specifically employed to ascertain friction force. Models 2, 3, and 4 are utilized to investigate the impact of cylinder radius r_1 on performance, while models 2, 5, and 6 are dedicated to exploring the influence of helical tube radius r_2. Lastly, the test involving models 2, 7, 8, and 9 primarily scrutinize the impact of helical tube length l. A total of 39 experimental conditions are designed. For each model, the loading forms include triangular and sinusoidal waves. The amplitude for the triangular wave loading is 30 mm (0.1 Hz), while for the sinusoidal wave, the amplitudes are 10 mm (2 Hz), 20 mm (1 Hz), and 30 mm (0.5 Hz). The purpose is to analyze the effect of different design parameters on the output of the inerter. Model 2 serves as the standard group, and its loading conditions include 10 mm (1 Hz, 2 Hz, 3 Hz), 20 mm (0.5 Hz, 1 Hz, 2 Hz), and 30 mm (0.1 Hz, 0.5 Hz, 1 Hz) to analyze the influence of different amplitudes and frequencies on the output of the inerter.

3.2. Verification of the theoretical model

Throughout the loading process, the primary output forces from the separated fluid inerter encompass friction force, inertial force, and parasitic damping force. This section aims to validate the theoretical model by comparing it with the experimental findings.

3.2.1. Coulomb friction force

Fig. 4 illustrates the Coulomb friction force between the piston and the inner wall of the hydraulic cylinder under loading conditions (IS315–5-4-TRI-empty). The behavior of this friction force aligns with Coulomb's law of friction (refer to Eq. (16)). Based on the experimental outcomes, an estimation suggests that the Coulomb friction force f approximately amounts to 55 N.

$$f = f_0 sign(\dot{x}) \tag{16}$$

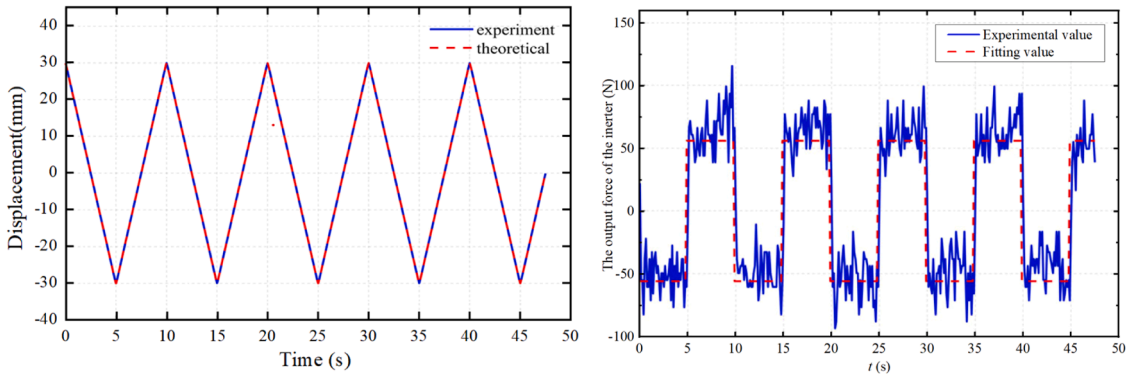

Fig. 4. The displacement and force-time curve of the inerter model (IS315–5-4-TRI-empty). (a) The displacement-time curve; (b) The force-time curve.

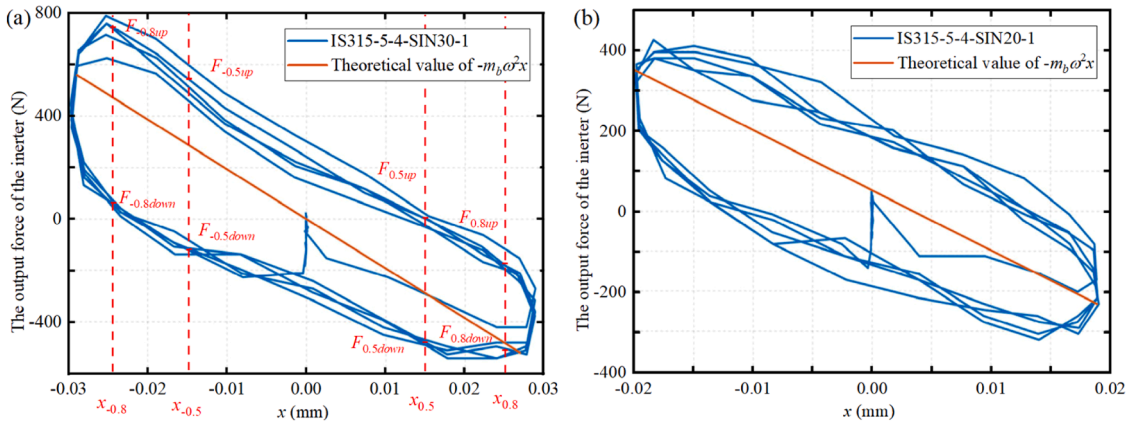

Fig. 5. Comparative analysis between theoretical and experimental results of $-m_b\omega^2$. (a) IS315–5-4-SIN30–1; (b) S315–5-4-SIN20–1.

Table 4
Comparative analysis between theoretical and experimental values of inertance m_b.

Case No.	Theoretical value	Experimental value	Relative error E_r
IS315 −5 −4-SIN30 −1	495	490	1.0 %
IS315 −5 −4-SIN10 −1	495	416	19.0 %
IS315 −5 −5-SIN30 −0.5	618	635	2.7 %
IS315 −10 −4-SIN20 −1	124	142	12.7 %
IS400 −5 −4-SIN30 −0.5	1286	1458	11.8 %

Where f is the Coulomb friction force, f_0 is the maximum static friction force.

3.2.2. Negative stiffness

The analysis focuses on the results obtained under sinusoidal loading conditions. The sinusoidal wave is mathematically expressed as:

$$x = A\sin(\omega t) \tag{17}$$

Hence, the expression for the output force of the fluid inerter model can be represented as:

$$F_d = m_b\ddot{x} = -m_b\omega^2 A\sin(\omega t) \tag{18}$$

Fig. 5 displays the force-displacement hysteresis curves acquired during specific test conditions. As per Eq. (18), $-m_b\omega^2$ represents the diagonal slope of the hysteresis curve. The orange line denotes the theoretically calculated value. The close proximity between the experimental hysteresis curve's diagonal slope and the theoretical estimation indicates a significant alignment. These results underscore the reliability of the simplified mechanical model applied to the separated fluid inerter.To further quantitatively ascertain the accuracy of this simplified model, the inertance m_b under select test conditions is derived from experimental data. Notably, the hysteresis curve takes on an approximate shuttle-shaped pattern distributed across the second and fourth quadrants. The diagonal slope of the hysteresis curve can be derived using the following equation:

$$\alpha = -m_b\omega^2 = -\frac{1}{4}\left(\begin{array}{l}\left|\frac{F_{-0.5up}-F_{0.8up}}{x_{-0.5}-x_{0.8}}\right| + \left|\frac{F_{-0.8up}-F_{0.5up}}{x_{-0.8}-x_{0.5}}\right| \\ +\left|\frac{F_{-0.5down}-F_{0.8down}}{x_{-0.5}-x_{0.8}}\right| + \left|\frac{F_{-0.8down}-F_{0.5down}}{x_{-0.8}-x_{0.5}}\right|\end{array}\right) \tag{19}$$

In this equation, $x_{-0.5}$, $F_{-0.5up}$ and $F_{-0.5down}$ represent the displacement at $-0.5\,A$ and the corresponding forces at the upper and lower ends of the hysteresis curve, respectively, as depicted in Fig. 5(a).

The calculated results, compared with theoretical values, are assessed for relative errors using Eq. (20), presented in Table 4. A comparison reveals a close proximity between the calculated results derived from experimental values and those predicted by the theoretical model. The relative errors amount to 1.0 %, 19.0 %, 2.7 %, 12.7 %, and 11.8 % respectively. These findings further validate the reasonableness of the simplified model.

$$E_r = \left|\frac{Y_{th}-Y_{\exp}}{Y_{\exp}}\right| \times 100\% \tag{20}$$

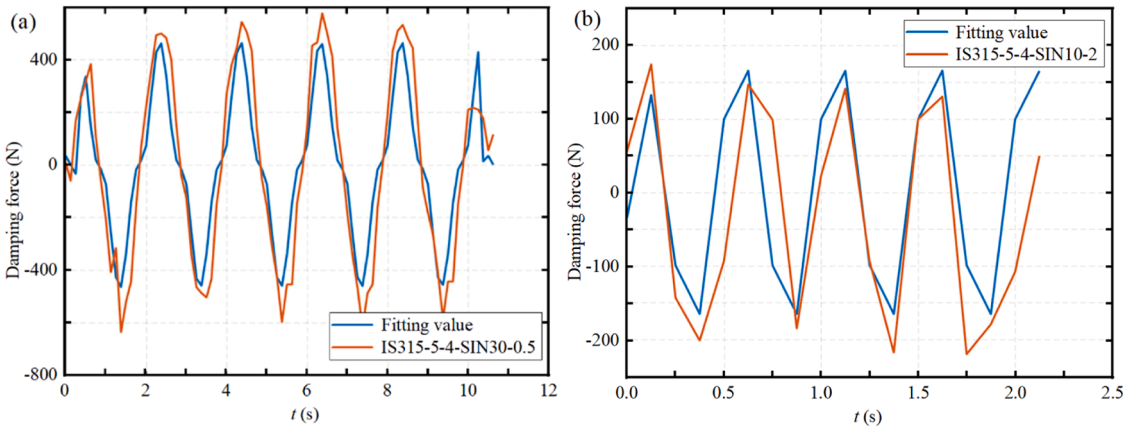

Fig. 6. Comparative analysis between fitting results and experimental data of damping force. (a) IS315–5-4-SIN30–0.5; (b) IS315–5-4-SIN10–2.

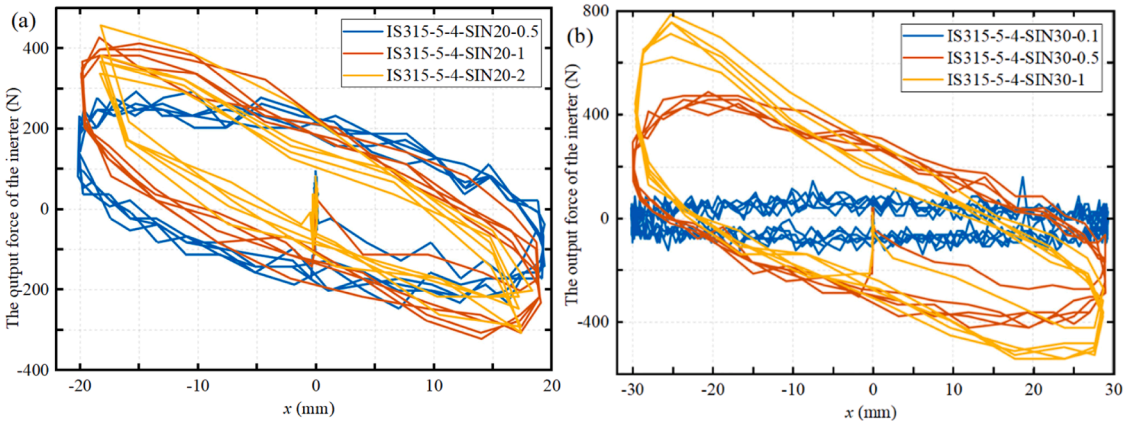

Fig. 7. Force-displacement hysteresis curves under various frequencies. (a) 0.5, 1 and 2 Hz; (b) 0.1, 0.5 and 1 Hz.

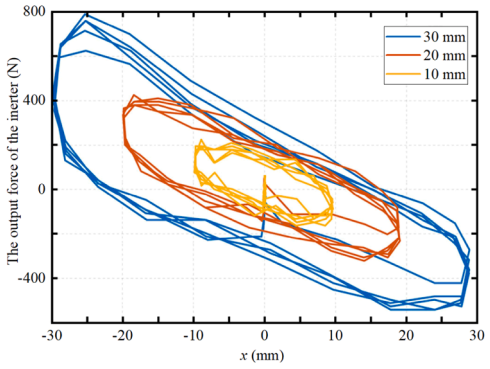

Fig. 8. Force-displacement hysteresis curves under varying amplitudes.

Where Y_{th} and Y_{exp} are theoretical and experimental values respectively.

3.2.3. Parasitic damping force

The pressure difference Δp is calculated by the pressure values at the inlet and outlet of the cylinders measured by the hydraulic sensor. The damping force F_d of the fluid inerter model is calculated utilizing Eq. (9) via experimental findings. Notably, due to varying test conditions, such as tube dimensions or material variations, theoretical damping coefficients c_1 and c_2 are derived from the empirical model may incur significant errors, especially at higher frequencies. Hence, to mitigate this, the damping coefficients are fitted based on Eq. (11) and experimental results [42]. For the determination of the fluid inerter's damping coefficients c_1 and c_2, the Gauss-Newton method and the least square method are employed for fitting, represented as:

$$\{c_1, c_2\} = \arg\min_{c_1, c_2} \sqrt{\sum_{i=1}^{N} \left\| F_{th}(i) - F_{\exp}(i) \right\|^2} \tag{21}$$

Where F_{th} and F_{exp} denote theoretical and experimental values, respectively.

Fig. 6 depicts the comparison between the fitting results, derived from the model introduced by White [36], and the experimental values of the damping force F_d. Despite localized discrepancies between the fitting results and the experimental values, the overall fitting effect remains satisfactory, consistent with the findings reported by Liu et al. [42].

3.3. The influence of loads with different amplitude and frequency

Fig. 7 illustrates the force-displacement hysteretic curves of the fluid inerter under varying loading frequencies. Notably, the observed hysteresis curves exhibit a plump, shuttle-shaped characteristic across these working conditions. The fluid inerter model showcases commendable energy dissipation capacity and performance stability. Remarkably, the output force of the fluid inerter model exhibits distinct behaviors with fluctuations in the loading frequency. At loading frequency of 0.1 Hz, the force-displacement hysteresis curve approximates a rectangular shape, indicating a smaller inertial force. Here, the fluid inerter model primarily manifests frictional and minimal damping forces (refer to Fig. 7(b)). As the loading frequency escalates, both the absolute value of

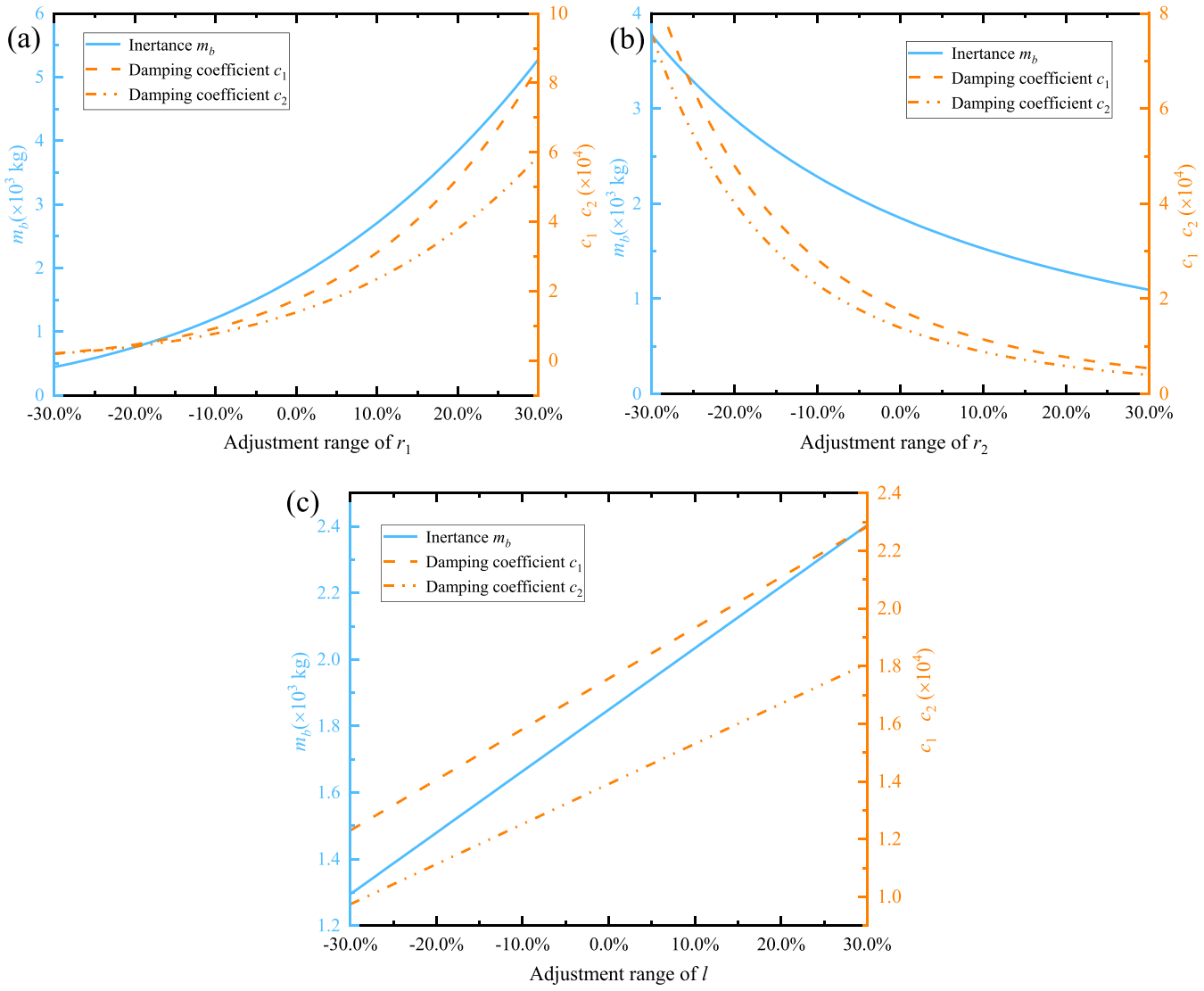

Fig. 9. Impact of various design parameters on fluid inerter performance. (a) The radius $r_1$of the cylinder; (b) The radius r_2 of the helical tube; (c) The length l of the helical tube.

the diagonal slope -$m_b\omega^2$ and the peak amplitude of the hysteresis curve proportionally increase, gradually adopting a plumper form. These findings underscore the inerter's capability to generate heightened inertial and damping forces under high-frequency loads.

Fig. 8 depicts the force-displacement hysteretic curves of the fluid inerter under varying loading amplitudes. It is worth noting that regardless of the amplitude change, the effect on the diagonal slope of the hysteresis curve (representing negative stiffness, -$m_b\omega^2$) is small. The effect of amplitude variation on negative stiffness requires further in-depth investigation. However, both the peak value and the area enclosed by the hysteresis curve demonstrate an increase proportional to the amplitude increment. Additionally, a noteworthy observation is the nonlinearity exhibited in the hysteresis curve under a 30 mm amplitude and 1 Hz loading frequency. This nonlinearity arises due to the fluid inerter model's nonlinear damping characteristics under high-frequency loads.

3.4. The influence of different design parameters

The prior section established the theoretical model's accuracy through experimental validation. This section delves into the analysis of the fluid inerter's performance concerning various design parameters, namely the hydraulic cylinder radius r_1, helical tube radius r_2, and helical tube length l. Employing a single variable analysis method, each of these pivotal parameters is systematically varied within a range of 70 % to 130 % from their initial values (r_1= 0.05 m, r_2= 0.01 m, n= 15, H= 0.010 m, ρ_s= 7850 kg/m^3, R= 0.10 m, r_p= 29.9 mm, h_d= 0.014 m, Δr= 0.1 mm, ρ= 1000 kg/m^3, L= 0.300 m, μ= 0.001 Pa·s). The metrics evaluated as performance indices include inertance m_b damping coefficients c_1 and c_2. Fig. 9 illustrates the impact of design parameters on the corresponding performance indices. As depicted in Fig. 9(a), there exists a positive correlation between the inertance m_b and damping coefficients c_1 and c_2 with the radius r_1 of the cylinder. This relationship demonstrates an exponential increase in both m_b and c_1 and c_2 as the radius r_1 escalates. Conversely, Fig. 9(b) indicates a negative correlation between the inertance m_b and damping coefficients c_1 and c_2 with the radius r_1 of the helical tube. Here, m_b and c_1 and c_2 display a diminishing trend in a power function with an increase in r_2. Moreover, the length l of the helical tube showcases a linear incremental relationship with m_b and c_1 and c_2 as shown in Fig. 9(c). These findings underscore that the separated fluid inerter's performance is notably more sensitive to variations in the cylinder radius r_1 and helical tube radius r_2 compared to alterations in the length l of the helical tube. Additionally, it's evident that the design parameters exert a more significant influence on

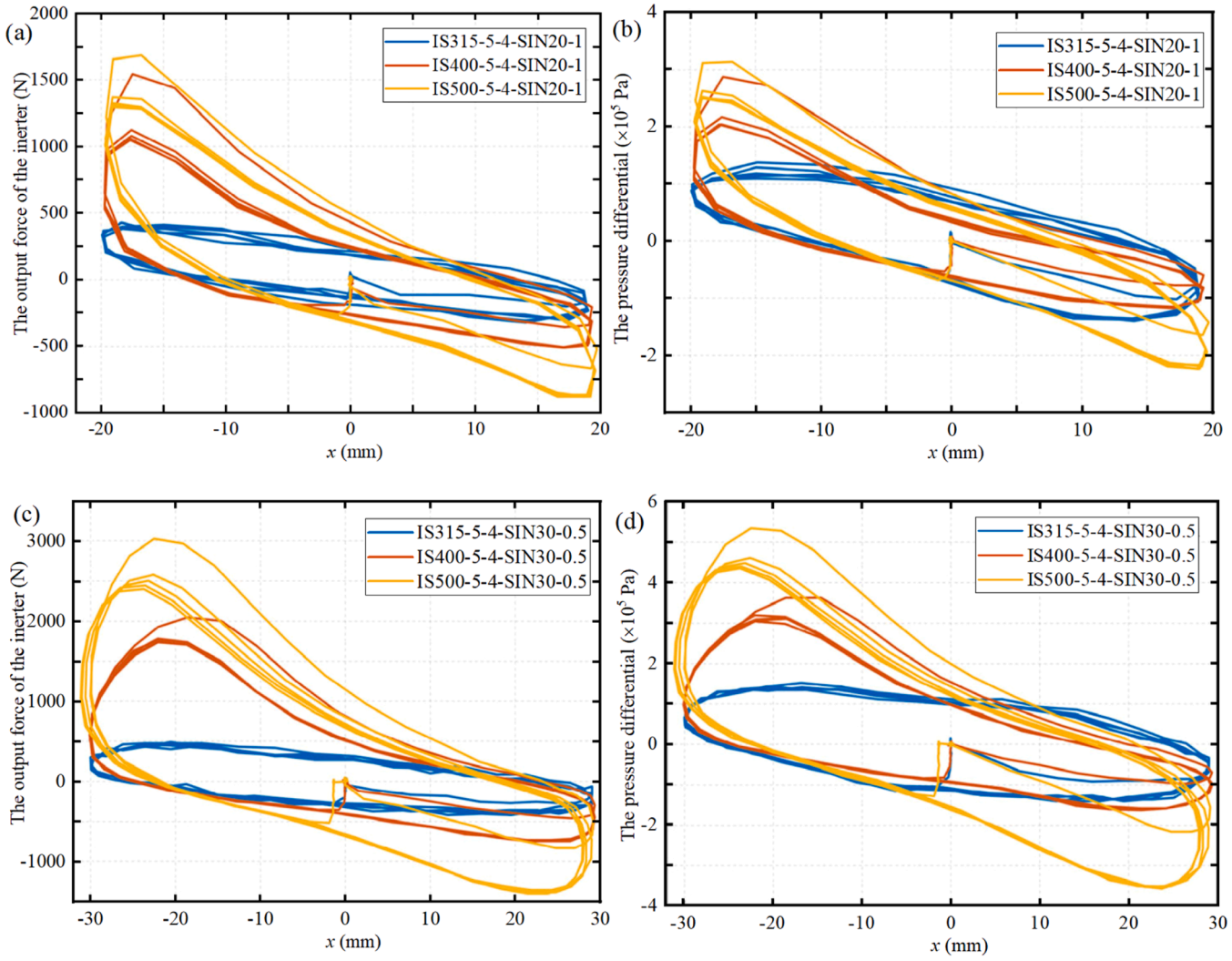

Fig. 10. Hysteresis curves of fluid inerter model with varied r_1. (a) Force-displacement curves (20 mm, 1 Hz); (b) Pressure difference-displacement curves (20 mm, 1 Hz); (c) Force-displacement curves (30 mm, 0.5 Hz); (d) Pressure difference-displacement curves (30 mm, 0.5 Hz).

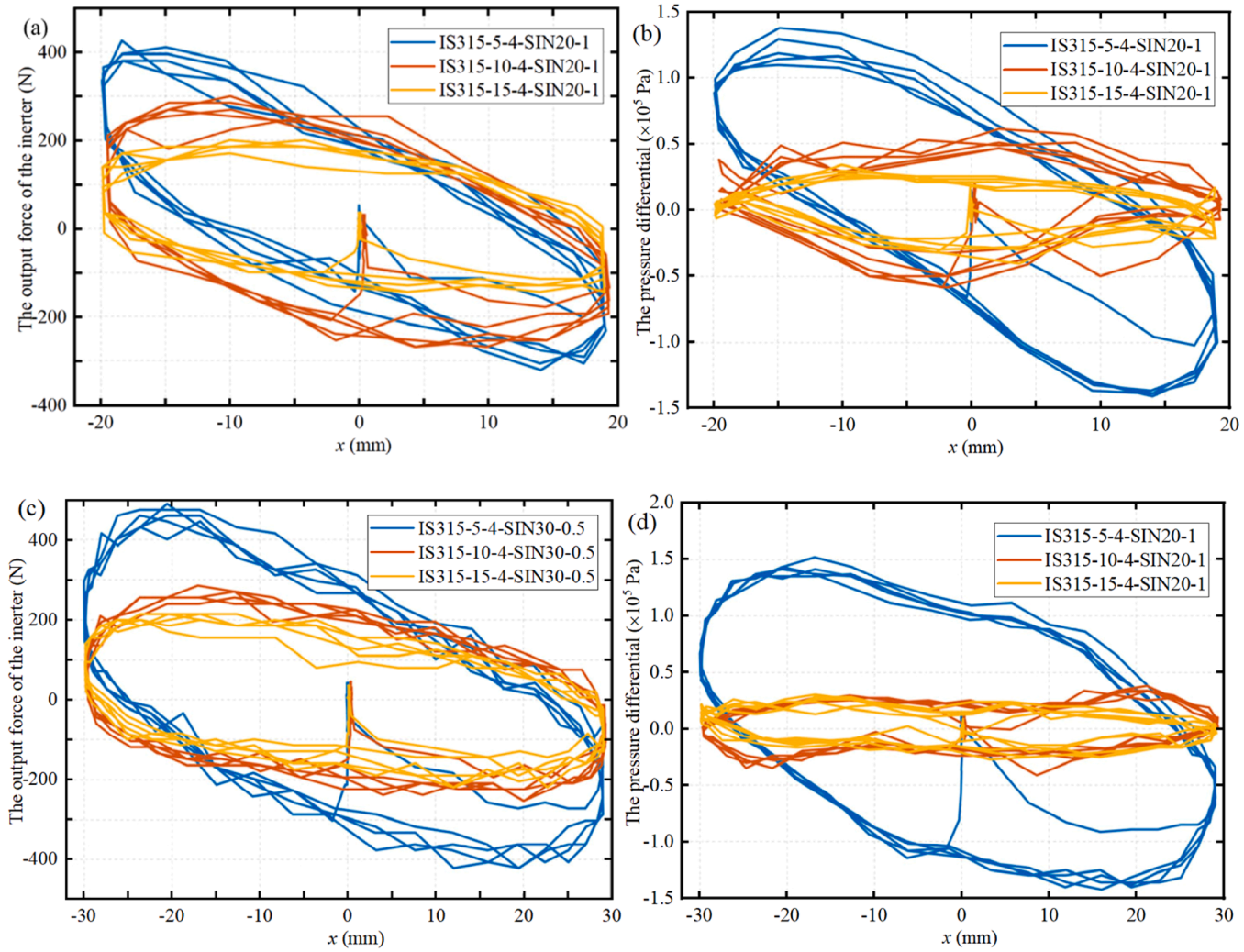

Fig. 11. Hysteresis curves of fluid inerter model with varied r_2. (a) Force-displacement curves (20 mm, 1 Hz); (b) Pressure difference-displacement curves (20 mm, 1 Hz); (c) Force-displacement curves (30 mm, 0.5 Hz); (d) Pressure difference-displacement curves (30 mm, 0.5 Hz).

damping coefficient c_1 than on damping coefficient c_2.

To delve deeper into understanding the impact of diverse design parameters on the fluid inerter's performance, a detailed analysis is conducted using the experimental outcomes. Figs. 10 to 12 present the force-displacement and pressure difference-displacement curves of the fluid inerter model with varying design parameters. The pressure difference across the helical tube's ends is extracted utilizing two hydraulic sensors.

Fig. 10 illustrates the force-displacement and pressure-displacement hysteresis curves of fluid inerter models with varying cylinder radii r_1 under two distinct test conditions (20 mm, 1 Hz and 30 mm, 0.5 Hz). As depicted in Fig. 10(a), there is a noticeable increase in both the diagonal slope and the area encompassed by the hysteresis curve as the hydraulic cylinder radius r_1 increases. This escalating trend becomes more pronounced under another test condition (30 mm and 0.5 Hz, depicted in Fig. 10(c)). Additionally, the peak output force of the inerter demonstrates a substantial increase with an augmented radius r_1.

Fig. 11 exhibits the hysteresis curves of fluid inerter models with various helical tube radii r_2. The alterations in r_2 significantly affect the peak value, diagonal slope, and area of the hysteresis curve, decreasing as r_2 increases. This behavior can be attributed to the inverse relationship between the radius of the helical tube and the flow velocity of the liquid inside. Consequently, an increased radius diminishes the fluid inerter model's energy dissipation capacity, thereby reducing its ability to provide inertial force. However, as depicted in Fig. 12, the hysteresis curves of fluid inerter models with different helical tube lengths l almost overlap. This observation suggests that the length l of the helical tube has a minimal effect on the fluid inerter's performance. These findings demonstrate a consistency between the experimental and theoretical outcomes.

4. Performance analysis based on shaking table test

4.1. Experimental details

In practical engineering applications, inerters are typically combined with dampers and springs to form an inerter system. To further investigate the performance of the separated fluid inerter, a shake table test was conducted on a frame structure equipped with the base isolation-fluid inerter (FS-BIFI). As shown in Fig. 13, the original structure is a three-story steel frame structure made of Q235 steel, with each story having a height of 950 mm. The dimensions of the floor slab are 1040 mm × 1040 mm × 20 mm. The frame columns have a rectangular cross-section, with individual dimensions of 80 mm (length) × 20 mm (width) × 930 mm (height). Both the column bases and the frame joints are connected using angle steel. The design parameters of the separated inerter are $r_1 = 31.5$ mm, $r_2 = 5$ mm and $l = 6$ m.

The shake table excitations are the *Loma Prieta* (near-field) and *San Fernando* (far-field) seismic waves, with corresponding amplitudes of 0.05 g, 0.1 g, and 0.2 g, all applied as unidirectional excitations (as

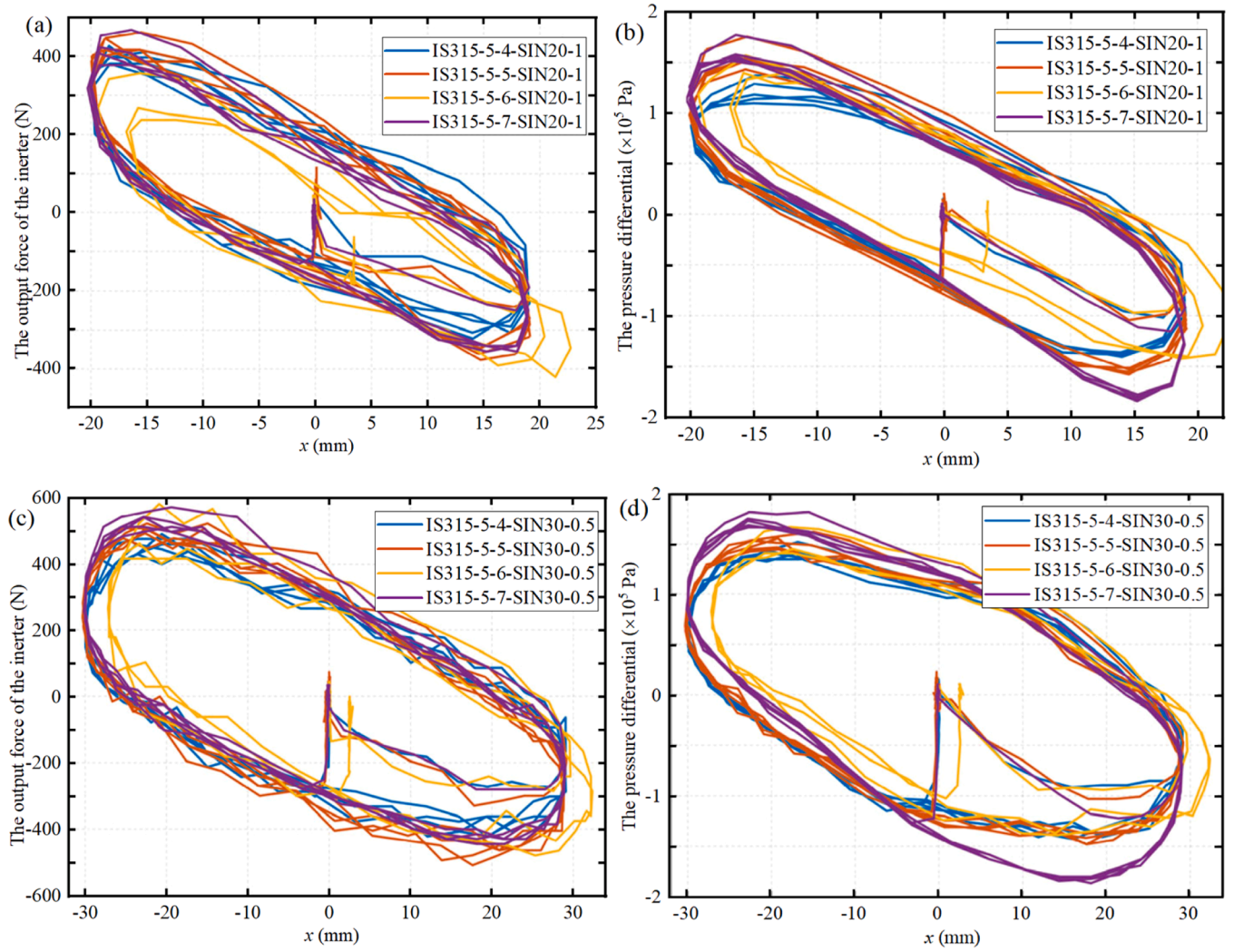

Fig. 12. Hysteresis curves of fluid inerter model with varied *l*. (a) Force-displacement curves (20 mm, 1 Hz); (b) Pressure difference-displacement curves (20 mm, 1 Hz); (c) Force-displacement curves (30 mm, 0.5 Hz); (d) Pressure difference-displacement curves (30 mm, 0.5 Hz).

shown in Fig. 14). The tests are conducted on the frame structure (FS), the frame structure equipped base isolation (FS-BI), and the FS-BIFI, with the test conditions summarized in Table 5. Based on the test data from the original structure, the stiffness and damping of the three-story frame structure are identified using the differential evolution (DE) algorithm [43]. The damping ratio of the upper frame structure is approximately 0.015, the inter-story stiffness is about 516.49 kN/m, and the first natural frequency is around 3 Hz. The stiffness of the isolation layer is approximately 49.12 kN/m, and the friction coefficient of the roller bearings is around 0.018. The experiment employed a unidirectional loading method, applying the load along the weak axis of the frame.

4.2. Result analysis

Fig. 15 shows the time history curves of the top floor acceleration and relative inter-story displacement for both the FS and the FS-BI under the *San Fernando* seismic wave (PGA= 0.10 g). It can be seen that, due to the effect of the base isolation layer, the time history responses of both the top floor acceleration and the relative inter-story displacement have been significantly suppressed. This indicates that base isolation has excellent seismic performance. Fig. 16 shows the time history curves of the isolation layer displacement and the top floor acceleration for FS-BI and FS-BIFI under the *Loma Prieta* and *San Fernando* earthquake waves (PGA=0.20 g). It can be seen that the presence of fluid inerter can further reduce the displacement of the isolation layer. However, its impact on the top floor acceleration of the structure is relatively small and may even amplify the top floor acceleration during certain time periods (e.g., Fig. 16 (a), 10–20 s).

To further analyze the performance of the separated fluid inerter, the peak amplitude and root mean square (RMS) value of the time history response are used as evaluation metrics. The peak amplitude represents the instantaneous response of the structure, while the RMS value represents the average response over the entire vibration period. Table 6 shows the peak amplitude and RMS value of displacement and acceleration for the FS, the FS-BI, and the FS-BIFI under different earthquake waves. Furthermore, the response reduction rate is used to analyze the seismic effect, which can be expressed as:

$$R = \frac{X_1 - X_2}{X_1} \times 100\% \tag{22}$$

Where, X_1 and X_2 represent the responses of the structure before and after reduction, respectively. The results of FS-BI are compared with those of FS, and the results of FS-BIFI are compared with those of FS-BI.

From Table 7, it can be seen that the FS-BI exhibits excellent isolation performance, significantly reducing both displacement and acceleration responses of the structure. Moreover, as the PGA increases, the isolation effect of the isolation layer improves. Additionally, it is observed that

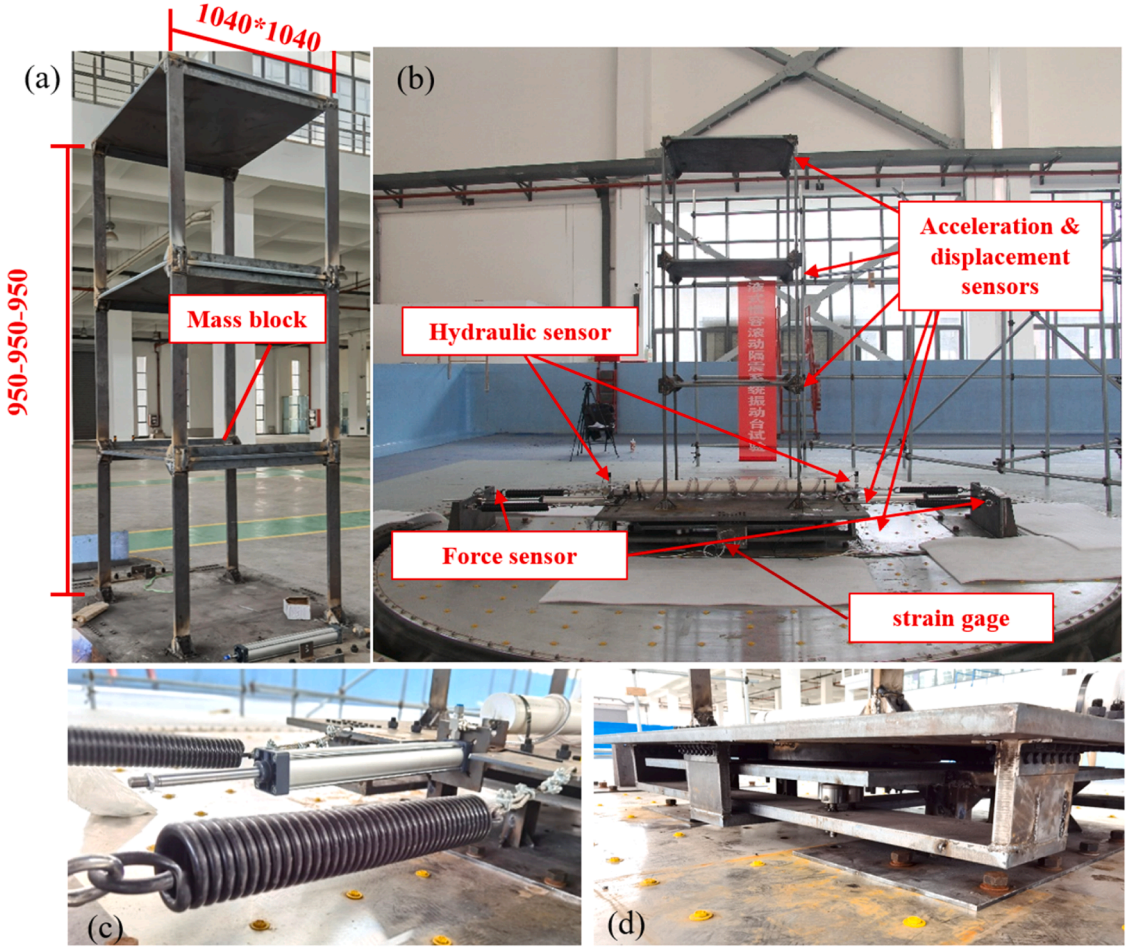

Fig. 13. Shaking table test. (a) The three-story steel frame structure; (b) The frame structure equipped with the base isolation-fluid inerter; (c) The separated fluid inerter; (d) The anti-overturning rolling isolation.

the response reduction rate of the FS-BI under the *Loma Prieta* (near-field) seismic wave is significantly higher than that under the *San Fernando* (far-field) seismic wave.

From Table 8, it can be seen that the addition of the fluid inerter can significantly and effectively reduce the displacement of the isolation layer. The response reduction rates for the peak value and the root mean square (RMS) value of the isolation layer displacement are 18.21 % and 23.37 %, respectively. However, it can amplify the top floor acceleration of the structure to some extent (−19.30 %), and the reduction rate varies under different earthquake excitations. Overall, as the PGA increases, the reduction rate of the top floor acceleration changes from negative to positive, meaning the effect shifts from amplification to reduction. Due to the limited number of conditions in this experiment, further in-depth research is needed.

5. Conclusions

This paper presentes a separated fluid inerter, which is composed of two separated hydraulic cylinders, a helical tube and two pistons. The construction and working principle of the separated fluid inerter are introduced, and its mechanical model is established. Experiments on the fluid inerter models with different design parameters under various loads are conducted to validate the accuracy of the mechanical model. In addition, the seismic performance of the frame structure equipped with the base isolation-fluid inerter (FS-BIFI) is investigated by shaking table test. The primary conclusions are summarized as follows:

(1) The introduced separated fluid inerter amplifies fluid velocity through a diameter difference between the helical tube and the hydraulic cylinder, generating significant inertia force and kinetic energy storage. The primary output forces consist of inertial force (F_{bch}) and damping force (F_d), mainly arising from fluid flow within the helical tube. The separated fluid inerter can be simplified as a parallel model comprising an inertance element (m_b) and nonlinear damping elements (c_1, c_2). Notably, the fluid inerter exhibits negative stiffness, with its inertia force lacking participation in energy dissipation; instead, its energy dissipation primarily stems from its inherent nonlinear damping.

(2) The theoretical model undergoes verification through diverse test conditions applied to the experiment of fluid inerter model. The experimental results for inertance closely align with theoretical results, revealing relative errors of 1.0 %, 19.0 %, 2.7 %, 12.7 %, and 11.8 %, respectively. The separated fluid inerter relies on three crucial design parameters: the cylinder radius (r_1), the helical tube radius (r_2), and the length of the helical tube (l). Notably, the inerter's performance exhibits considerable sensitivity to alterations in both the cylinder radius (r_1) and the helical tube radius (r_2).

(3) The FS-BI exhibits excellent isolation performance, significantly reducing both displacement and acceleration responses of the structure. The addition of the fluid inerter can significantly and effectively reduce the displacement of the isolation layer. Compared with the results of FS-BI, The response reduction rates of FS-BIFI for the peak value and the root mean square (RMS) value of the isolation layer displacement are 18.21 % and

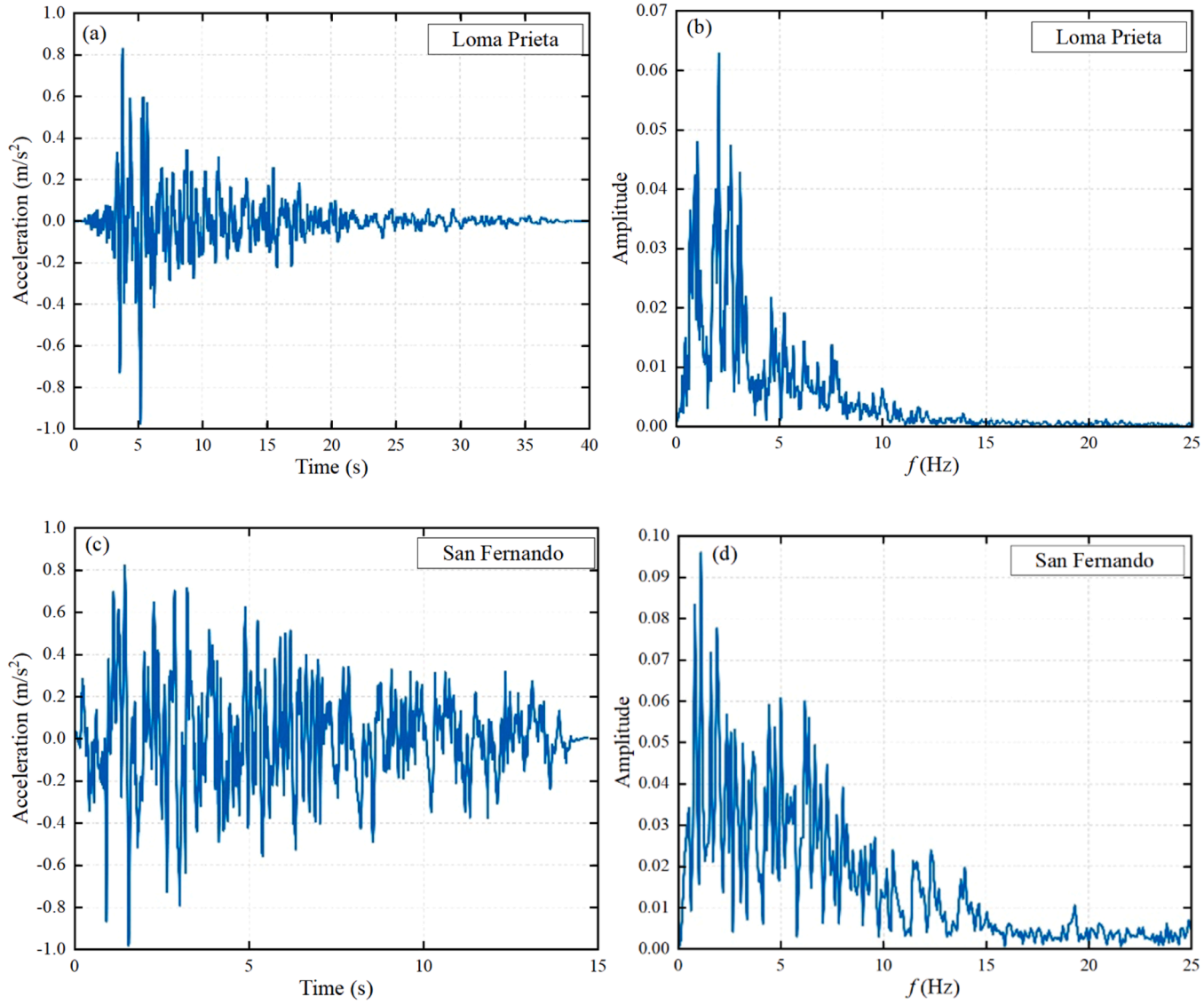

Fig. 14. Seismic acceleration and corresponding frequency spectrum. (a) *Loma Prieta*, acceleration; (b) *Loma Prieta*, frequency; (c) *San Fernando*, acceleration; (d) *San Fernando*, frequency.

Table 5
Test conditions of shaking table.

Model	Seismic excitation	PGA (g)
FS	Loma Prieta	0.05
		0.10
	San Fernando	0.05
		0.10
FS-BI	Loma Prieta	0.05
		0.10
		0.20
	San Fernando	0.05
		0.10
		0.20
FS-BIFI	Loma Prieta	0.05
		0.10
		0.20
	San Fernando	0.05
		0.10
		0.20

23.37 %, respectively. However, it can amplify the top floor acceleration of the structure to some extent (−19.30 %), and the reduction rate varies under different earthquake excitations.

Despite its perceived advantages in simplicity and durability, the practical utilization of the separated fluid inerter remains limited, and its actual impact in real-world engineering applications requires further investigation. Furthermore, the current analysis of the separated fluid inerter primarily focuses on its attributes as a two-terminal element. To fully exploit the potential advantages of the separated inerter, exploring the efficacy of a multi-terminal separated fluid inerter in future studies could offer valuable insights.

CRediT authorship contribution statement

Hesheng Tang: Writing – review & editing, Writing – original draft, Project administration, Methodology, Funding acquisition, Data curation, Conceptualization. **Taikun Guo:** Writing – original draft, Investigation, Formal analysis, Conceptualization. **Yangyang Liao:** Writing – original draft, Supervision, Methodology, Investigation, Formal analysis, Conceptualization. **Rongshuai Li:** Writing – review & editing,

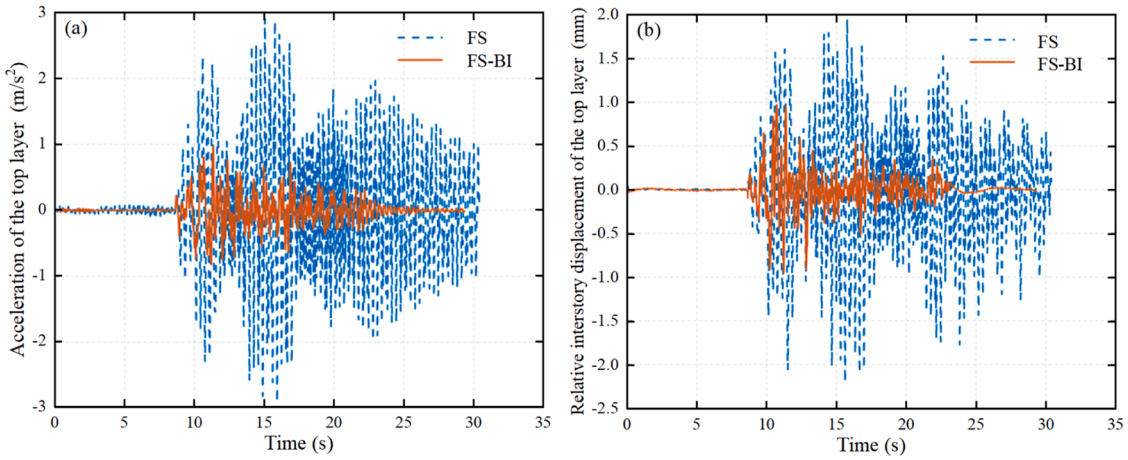

Fig. 15. The time history curves of the top floor acceleration and relative inter-story displacement for both the FS and the FS-BI (PGA=0.1 0 g). (a) *San Fernando*, acceleration; (b) *San Fernando*, displacement.

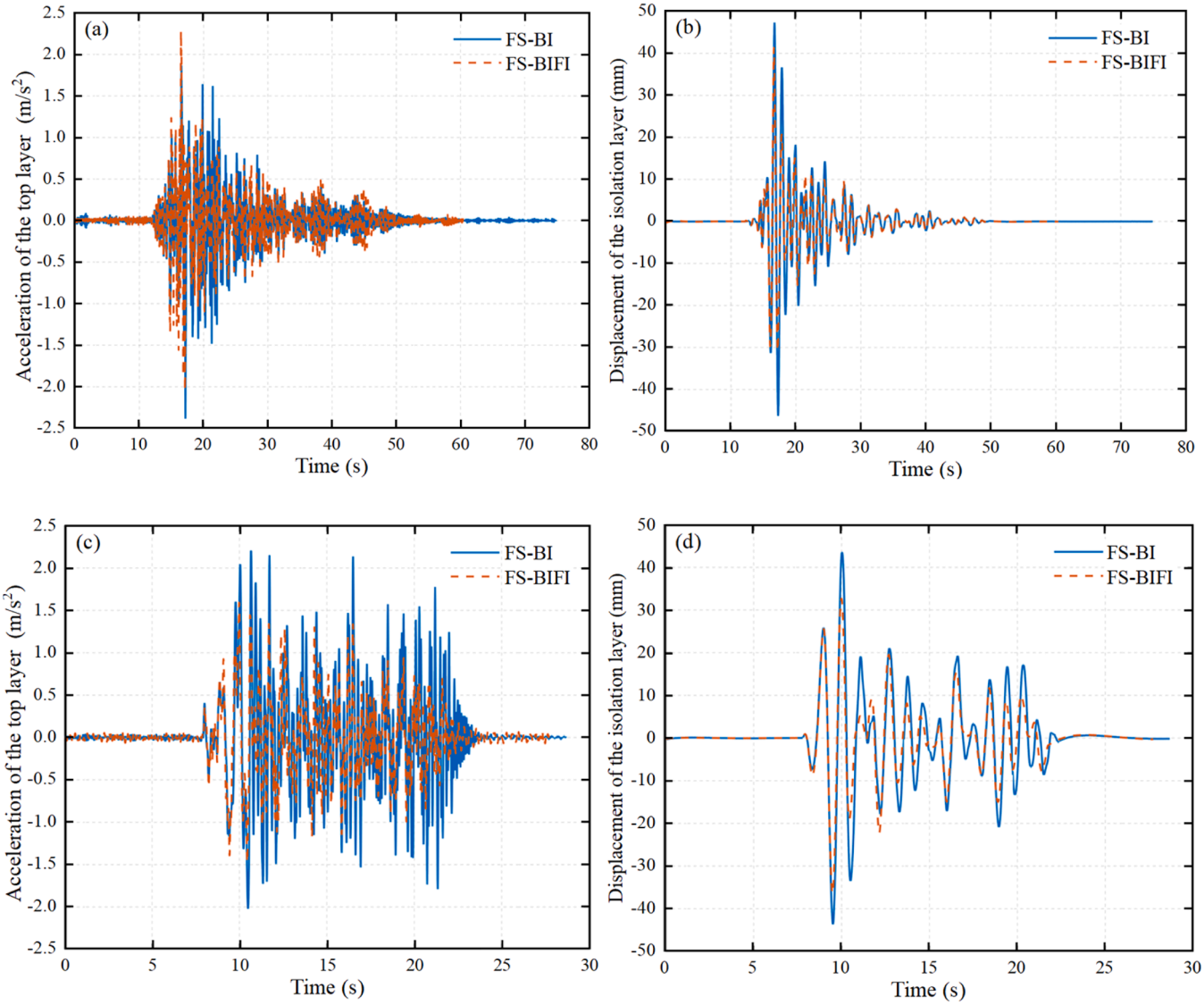

Fig. 16. The time history curves of the isolation layer displacement and the top floor acceleration for FS-BI and FS-BIFI (PGA=0.20 g). (a) *Loma Prieta*, acceleration; (b) *Loma Prieta*, displacement; (c) *San Fernando*, acceleration; (d) *San Fernando*, displacement.

Table 6
The peak amplitude and RMS value of displacement and acceleration for the FS, the FS-BI, and the FS-BIFI.

Model	Seismic excitation	PGA (g)	Acceleration of the top layer (m/s^2)		The relative acceleration of the top layer (m/s^2)		Displacement of top layer (mm)		Displacement of isolation layer (mm)	
			Max	RMS	Max	RMS	Max	RMS	Max	RMS
Three-story frame structure	Loma Prieta	0.05 g	2.3448	0.7306	2.2567	0.6952	9.8970	1.6898	-	-
		0.10 g	4.8139	1.4214	4.7865	1.3634	20.6899	4.0739	-	-
	San Fernando	0.05 g	1.6409	0.4515	1.5591	0.4072	5.4927	1.3493	-	-
		0.10 g	3.3682	0.8741	3.2783	0.7999	11.7251	2.8559	-	-
Three-story frame structure equipped base isolation	Loma Prieta	0.05 g	0.6304	0.1115	0.6295	0.0873	8.8412	1.1708	7.5794	0.9646
		0.10 g	1.1816	0.1692	1.1197	0.1348	20.4835	2.7809	17.1943	2.3381
		0.20 g	2.4973	0.2796	1.6646	0.2118	55.4302	6.7970	47.6215	5.9200
	San Fernando	0.05 g	0.8682	0.1677	0.7722	0.1336	7.3459	1.4443	5.7583	1.1550
		0.10 g	1.2332	0.2098	1.1262	0.1584	21.6645	4.1073	17.5198	3.4031
		0.20 g	2.3171	0.5853	2.1781	0.4402	53.7666	11.1960	43.2888	9.4939
FS-BIFI	Loma Prieta	0.05 g	0.7286	0.1212	0.7076	0.0990	7.8437	1.0162	6.9239	0.8537
		0.10 g	1.4096	0.1807	1.3343	0.1424	19.9271	2.6539	17.6797	2.2604
		0.20 g	2.3727	0.2927	1.8320	0.2301	45.6817	6.0097	39.5481	5.1740
	San Fernando	0.05 g	0.8004	0.1802	0.7715	0.1425	7.1174	1.4210	5.3719	1.1400
		0.10 g	1.2203	0.2123	1.1385	0.1600	16.9152	3.0754	14.3295	2.6077
		0.20 g	1.7463	0.3953	1.4233	0.2861	43.3778	8.7426	36.2097	7.3752

Table 7
The reduction rate of structural response to BI (FS-BI & FS).

Seismic excitation	PGA (g)	$R_{a,\ max}$	$R_{a,\ rms}$	$R_{x1,\ max}$	$R_{x1,\ rms}$
Loma Prieta	0.05	73.12 %	84.73 %	66.72 %	58.85 %
	0.10	75.46 %	88.10 %	69.37 %	77.29 %
San Fernando	0.05	47.09 %	62.87 %	36.35 %	33.61 %
	0.10 g	63.39 %	76.00 %	48.06 %	62.65 %

Note: R_a is the top layer acceleration reduction rate , R_{x1} is the top relative interlayer displacement reduction rate.

Table 8
The reduction rate of structural response to BIFI (FS-BIFI & FS-BI).

Seismic excitation	PGA (g)	$R_{a,\ max}$	$R_{a,\ rms}$	$R_{x2,\ max}$	$R_{x2,\ rms}$
Loma Prieta	0.05	−15.58 %	−8.67 %	8.65 %	11.50 %
	0.10	−19.30 %	−6.83 %	2.82 %	3.32 %
	0.20	4.99 %	−4.70 %	16.95 %	12.60 %
San Fernando	0.05	7.82 %	−7.50 %	6.71 %	1.30 %
	0.10	1.04 %	−1.22 %	18.21 %	23.37 %
	0.20	24.64 %	32.47 %	16.35 %	22.32 %

Note: R_a is the top layer acceleration reduction rate , R_{x2} is the isolation layer displacement reduction rate.

Supervision, Investigation. **Liyu Xie:** Writing – original draft, Formal analysis.

Declaration of Competing Interest

The authors declare that they have no known competing financial interests or personal relationships that could have appeared to influence the work reported in this paper.

Acknowledgments

This research was supported by the National Key R&D Program of China (Grant No. 2021YFE0112200), Ministry of Science and Technology of China (Grant No. SLDRCE19-B-02), and National Natural Science Foundation of China (Grant No. 52378184).

References

[1] Formisano A., Chieffo N., Asteris P.G., Lourenço, P.B. Seismic risk scenario for the historical centre of castelpoto in Southern Italy. Earthquake Engineering & Structural Dynamics, 2023.
[2] Otárola K, Gentile R, Sousa L, Galasso C. Accounting for earthquake-induced ground-motion duration in building-portfolio loss assessment. Earthq Eng Struct Dyn 2023;52(4):887–909.
[3] Xu ZD. Earthquake mitigation study on viscoelastic dampers for reinforced concrete structures. J Vib Control 2007;13(1):29–43.
[4] Xu K, Dai Q, Bi K, Fang G, Zhao L. Multi-mode vortex-induced vibration control of long-span bridges by using distributed tuned mass damper inerters (DTMDIs). J Wind Eng Ind Aerodyn 2022;224:104970.
[5] Xu Y, Xu ZD, Hu H, Guo YQ, Huang XH, Zhang ZW, et al. Experiment, simulation, and theoretical investigation of a new type of interlayer connections enhanced viscoelastic damper. Int J Struct Stab Dyn 2024:2550045.
[6] Cui GP, Feng LH, Hu YW. Flow-induced vibration control of a circular cylinder by using flexible and rigid splitter plates. Ocean Eng 2022;249:110939.
[7] You T, Zhou J, Thompson DJ, Gong D, Chen J, Sun Y. Vibration reduction of a high-speed train floor using multiple dynamic vibration absorbers. Veh Syst Dyn 2022; 60(9):2919–40.
[8] Lu Y, Liao Y, Xu W. An investigation into the fatigue damage of a long flexible cylinder with multiple control rods in crossflow. Ocean Eng 2020;202:107175.
[9] Chen X, Xiong J. Seismic resilient design with base isolation device using friction pendulum bearing and viscous damper. Soil Dyn Earthq Eng 2022;153:107073.
[10] Xu ZD, Liao YX, Ge T, Xu C. Experimental and theoretical study of viscoelastic dampers with different matrix rubbers. J Eng Mech 2016;142(8):04016051.
[11] Sun H, Fang P, Peng H, Zou M, Xu Y. Theoretical, numerical and experimental studies on double-frequency synchronization of three exciters in dynamic vibration absorption system. Appl Math Model 2022;111:384–400.
[12] Sadan B. State of the Art in Application of Seismic Isolation and Energy Dissipation in Turkey Seismic Isolation. Energy Dissipation and Active Vibration Control of Structures: 17th World Conference on Seismic Isolation (17WCSI. Cham: Springer International Publishing,; 2023. p. 17–25.
[13] Sun J, Zhufu G. Mechanical behavior of laminated rubber isolation bearing with buckling steel plate. Int J Steel Struct 2022;22(4):1069–85.
[14] Jaisee S, Yue F, Ooi YH. A state-of-the-art review on passive friction dampers and their applications. Eng Struct 2021;235:112022.
[15] Xu Y, Xu ZD, Guo YQ, Ge T, Xu C, Huang X. Theoretical and experimental study of viscoelastic damper based on fractional derivative approach and micromolecular structures. J Vib Acoust 2019;141(3):031010.
[16] Xu Y, He Q, Guo YQ, Huang XH, Dong YR, Hu ZW, et al. Experimental and theoretical investigation of viscoelastic damper by applying fractional derivative method and internal variable theory. Buildings 2023;13(1):239.
[17] Xu Y, Xu ZD, Guo YQ, Jia H, Huang X, Wen Y. Mathematical modeling and test verification of viscoelastic materials considering microstructures and ambient temperature influence. Mech Adv Mater Struct 2022;29(28):7063–74.
[18] Xu Y, Xu ZD, Guo YQ, Sarwar W, She W, Geng ZF. Study on viscoelastic materials at micro scale pondering supramolecular interaction impacts with DMA tests and fractional derivative modeling. J Appl Polym Sci 2023;140(13):e53660.
[19] He Q, Xu ZD, Xu Y, Guo YQ, Huang XH, Dong YR, et al. Mechanical and damping properties analyses of small molecular modifiers/nitrile-butadiene rubber composite: molecular dynamics simulation. Macromol Theory Simul 2023;32(1): 2200051.
[20] Rahimi F, Aghayari R, Samali B. Application of tuned mass dampers for structural vibration control: a state-of-the-art review. Civ Eng J 2020:1622–51.
[21] Zhang R, Zhao Z, Dai K. Seismic response mitigation of a wind turbine tower using a tuned parallel inerter mass system. Eng Struct 2019;180:29–39.
[22] Ma R, Bi K, Hao H. Inerter-based structural vibration control: a state-of-the-art review. Eng Struct 2021;243:112655.
[23] Ikago K., Sugimura Y., Saito K., Inoue N. Optimum seismic response control of multiple degree of freedom structures using tuned viscous mass dampers.

Proceedings of the 10th International Conference on Computational Structures Technology. Stirlingshire, Scotland. 2010.
[24] Ikago K., Saito K., Inoue N. Optimum multi-modal seismic control design of high-rise buildings using tuned viscous mass dampers. Proceedings of the 13th International Conference on Civil, Structural and Environmental Engineering Computing. Chania, Crete, Greece. 2011.
[25] Saito K, Kurita S, Inoue N. Optimum response control of 1-DOF system using linear viscous damper with inertial mass and its Kelvin-type modeling. J Struct Eng 2007;53:53–66.
[26] Zhang R, Zhao Z, Pan C, Ikago K, Xue S. Damping enhancement principle of inerter system. Struct Control Health Monit 2020;27(5):e2523.
[27] Shen Y, Chen L, Liu Y, Zhang X, Yang X. Optimized modeling and experiment test of a fluid inerter. J Vibroengineering 2016;18(5):2789–800.
[28] Smith MC, Wang FC. Performance benefits in passive vehicle suspensions employing inerters. Veh Syst Dyn 2004;42(4):235–57.
[29] Ikago K, Saito K, Inoue N. Seismic control of single-degree-of-freedom structure using tuned viscous mass damper. Earthq Eng Struct Dyn 2012;41(3):453–74.
[30] Zhang L, Xue S, Zhang R, Hao L, Pan C, et al. A novel crank inerter with simple realization: Constitutive model, experimental investigation and effectiveness assessment. Eng Struct 2022;262:114308.
[31] Wang FC, Hong MF, Lin TC. Designing and testing a hydraulic inerter. Proc Inst Mech Eng, Part C J Mech Eng Sci 2011;225(1):66–72.
[32] Swift SJ, Smith MC, Glover AR, Papageorgiou C, Gartner B, et al. Design and modelling of a fluid inerter. Int J Control 2013;86(11):2035–51.
[33] Liu C, Chen L, Zhang X, Yang Y, Nie J. Design and tests of a controllable inerter with fluid-air mixture condition. IEEE Access 2020;8:125620–9.
[34] Massey BS, Ward-Smith J. Mechanics of Fluids. Crc Press,; 1998.
[35] Rodman S, Trenc F. Pressure drop of laminar oil-flow in curved rectangular channels. Exp Therm Fluid Sci 2002;26(1):25–32.
[36] White CM. Fluid friction and its relation to heat transfer. Trans Inst Chem Eng 1932;10:66–86.
[37] Mishra P, Gupta SN. Momentum transfer in curved pipes. 1. Newtonian fluids. Ind Eng Chem Process Des Dev 1979;18(1):130–7.
[38] Shen Y, Chen L, Liu Y, Zhang X. Modeling and optimization of vehicle suspension employing a nonlinear fluid inerter. Shock Vib 2016;2016.
[39] De Domenico D, Deastra P, Ricciardi G, Sims ND, Wagg DJ. Novel fluid inerter based tuned mass dampers for optimised structural control of base-isolated buildings. J Frankl Inst 2019;356(14):7626–49.
[40] Itō H. Friction factors for turbulent flow in curved pipes. J Basic Eng 1959;81(2):123–32.
[41] Kubair V, Varrier CBS. Pressure drop for liquid flow in helical coils. Trans Indian Inst Chem Eng 1962;14:93–7.
[42] Liu X, Jiang JZ, Titurus B, Harrison A. Model identification methodology for fluid-based inerters. Mech Syst Signal Process 2018;106:479–94.
[43] Pant M, Zaheer H, Garcia-Hernandez L, et al. Differential evolution: a review of more than two decades of research. Eng Appl Artif Intell 2020;90:103479.